Surface & Coatings Technology 366 (2019) 41–53

Contents lists available at ScienceDirect

Surface & Coatings Technology

journal homepage: www.elsevier.com/locate/surfcoat

Enhanced discharge and surface properties of (Ti,AlCr)N coatings by cleaning cathodic-arc chamber

Ying Kong[a], Xiubo Tian[a,*], Chunzhi Gong[a], Dmitriy A. Golosov[b], Muqin Li[c], Qinwen Tian[a]

[a] State Key Laboratory of Advanced Welding and Joining, Harbin Institute of Technology, Harbin 150001, China
[b] Thin Film Research Laboratory, Belarussian State University of Informatics and Radioelectronics, Minsk, Belarus
[c] School of Materials Science & Engineering, Jiamusi University, Jiamusi 154007, China

ARTICLE INFO

Keywords:
Cathodic arc discharge
Cleaned chamber
(Ti,AlCr)N coatings
Deposition rate
Surface properties

ABSTRACT

In the PVD processes, the clearance of the chamber wall directly affects the microstructure and surface properties of the coatings. The (Ti,AlCr)N coatings are fabricated on M2 high-speed steel (HSS) and Si (100) by cathodic arc evaporation with the vacuum chamber cleaned or uncleaned. With the chamber cleaned, the arc discharge was enhanced with a higher intensity of optical spectrum and the concentration of residual oxygen was decreased. The clearance of chamber wall altered the external behavior of power supply and a larger input power was achieved. The average substrate ion current was increased by 13.0% and a larger E_{bi} was observed implying increased densification of coatings. A thicker coating was obtained with less surface defects (macroparticles). Consequently the microstructure and surface properties of (Ti,AlCr)N coatings have been improved with higher hardness, lower friction coefficient and superior adhesion strength between the coatings and substrate.

1. Introduction

The increasing application of high-speed dry cutting requires more comprehensive hard coating systems with low friction and high thermal properties. TiAlN and CrAlN are widely used as protective coatings for cutting tools to improve their performance [1,2]. The TiAlN coating with supersaturated face-centered cubic structure can provide glorious hardness and thermal stability. In particular, the spinodal decomposition of *c*-TiAlN into nano-sized Ti- and Al-rich domains leads to the self-hardening effect under thermal load, which has been successfully applied to machining tools [3]. CrAlN is another prominent protective coating due to the outstanding tribological properties and resistance to oxidation. The appearance of dense oxide during exposure to air at elevated temperatures effectively retards growth kinetics of the oxide scale [4–6], which is responsible for exceptional oxidation resistance. Therefore, the (Ti, AlCr)N coatings have frequently attracted great attention, because of its potential to combine the self-hardening effect of TiAlN and outstanding oxidation resistance of CrAlN [7–8].

Among the reported deposition technologies, cathodic arc evaporation (CAE) is featured by several remarkable advantages over competitive physical vapor deposition techniques (e.g., sputtering and hollow cathode evaporation), giving rise to its importance and popularity in industrially-scaled synthesis of protective coatings [9–11]. Apart from high evaporation rates and degree of ionization of target materials, the CAE's flexibility in terms of accessible material systems including metallic coatings, nitrides and oxides, represents an important key factor. During deposition processes, the microstructure and surface properties of the deposited films are determined by instrumental parameters including bias voltage [12], gas pressure [13], temperature [14], heat treatment [15], etc. In fact, these investigations have been widely reported in the numerous literatures. Besides the mentioned processing parameters, there are some other factors that cannot be ignored. Proper plasma cleaning (pre-deposition plasma treatment) effectively removes impurities from substrate surface and promotes good bonding, while excessive bombardment imparts more kinetic energy and causes peeling off due to residual stress [16]. Water vapor may stem from the residual atmosphere of the deposition chamber and the surroundings. They may be dissolved inside the deposited coatings, contaminate the surfaces and interfaces, and deteriorate the properties of coatings [17]. The position of the gas introduction into the chamber may affect the surface state and roughness of the substrates in the etching stage and the adhesion between the film and substrate. When gas is introduced near the arc source, the substrate surface is not rough relatively. In contrast, when gas is injected in the vicinity of the substrate, the substrate surface is rough [18]. The periodic variations in plasma density and fluxes of film-forming species may be produced by substrate rotation. This is utilized to modulate composition (e.g., nano-layer) and has drastic implications for the

* Corresponding author.
E-mail address: xiubotian@163.com (X. Tian).

https://doi.org/10.1016/j.surfcoat.2019.03.026
Received 31 August 2018; Received in revised form 10 March 2019; Accepted 12 March 2019
Available online 14 March 2019
0257-8972/

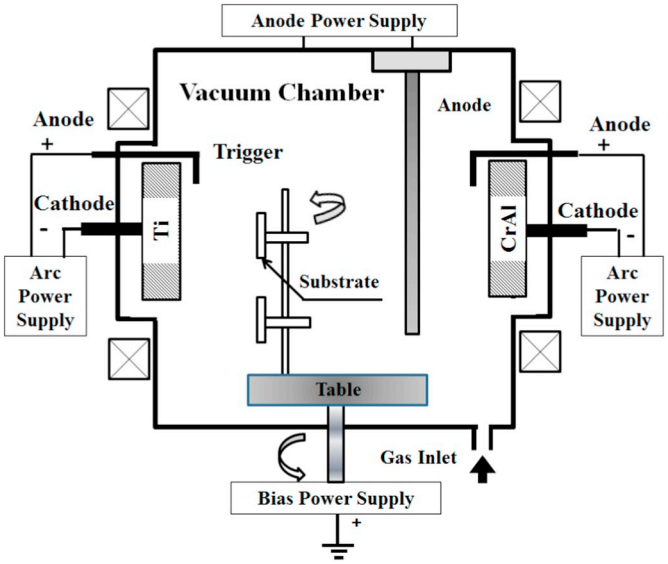

Fig. 1. Schematic diagram of cathodic arc system.

Table 1
Deposition parameters for (Ti,AlCr)N coatings.

	(Ti,AlCr)N coatings			
Target-substrate distance (mm)	250	300	350	400
N_2 flow rate (sccm)	500			
Base pressure (Pa)	3×10^{-3}			
Ti and AlCr target current (A)	100/100			
Substrate bias voltage(V)	–30			
Plasma etching	Ar plasma for 45 min at 1.5 Pa under substrate bias −200 V			
Substrate temperature (°C)	400			
Deposition time (min)	120			

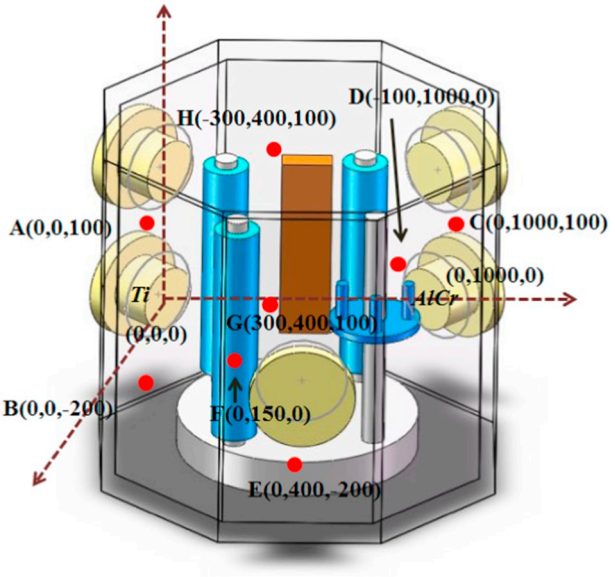

Fig. 2. Resistance measurement at different sites of chamber wall.

properties of coatings [19]. And, by adjusting the substrate position in the chamber, the lenticular-like fine grains, high density of micro twins, and better mechanical properties of coating can be achieved [20]. Similarly, the micro-blasting in the post treatment can induce residual compressive stresses to shift, which enhances tribological properties and the fracture resistance [21]. Of them, the effect of chamber-cleaning has been seldom reported although the chamber wall has to be cleaned regularly.

Table 2
Surface resistance of chamber with different conditions.

Plasma conditions	Resistance (Ω)							
	A	B	C	D	E	F	G	H
Uncleaned	75.6	61.2	889.3	863.4	20.4	11.7	1023.0	1104.1
Cleaned	2.2							

In this paper the (Ti,AlCr)N coatings were fabricated by cathodic arc evaporation (CAE) and two groups of experiments have been conducted. The first group of coating was deposited with the chamber cleaned and the second group was conducted with the chamber uncleaned. The substantial influence of chamber cleaning on the microstructure and mechanical properties of the coatings has been observed.

2. Experimental details

The (Ti,AlCr)N coatings were deposited on polished Si (100) and M2 high speed steel samples. The schematic diagram of the system used to deposit (Ti,AlCr)N coatings was shown in Fig. 1. The pure Ti (99.95%) and AlCr (99.95%) were utilized as targets. Substrates, (100)-oriented Si stripes and M2 high speed steel (Φ20mm × 4 mm) were ultrasonically cleaned in ethanol. After rinsing in distilled water and drying by hot air, the specimens were placed on the two-fold rotating carousel, which kept the rotation speed of 1.5 rpm. After the chamber was evacuated below 3×10^{-3} Pa and the temperature reached 400 °C, the high pure (99.999%) Ar gas was introduced to keep a pressure of 1.5 Pa. The specimens were cleaned by arc-enhanced plasmas with pulsed bias voltage of 200 V for 45 min in order to remove the native oxide layers and contaminations from the substrates. After the above ion-etching process, the Ti and TiN interlayer were deposited for 15 min and 25 min respectively to improve the adhesion between the films and substrate. Then high pure (99.999%) nitrogen was added as reactive gas with constant pressure of 3 Pa. The Ti and AlCr targets were evaporated with arc current of 100 A. The cathodic arc deposition lasted 120 min for two groups of experiments with the chamber cleaned and uncleaned. During the deposition, the carousel was biased with $V_p = -30$ V, pulsed frequency of 40 kHz, and duty cycle of D = 75%. Two groups of (Ti,AlCr)N coatings were deposited with target-substrate distance of 250 mm, 300 mm, 350 mm, 400 mm respectively. The detailed deposition parameters are listed in Table 1.

The substrate current was measured using a Tektronix digital oscilloscope via current sensor for the whole table assembly including the samples and holder. The optical emission signal was detected by a miniature fiber optic spectrometer AvaSpec-2048FT-4-DT, which was connected with the quartz fiber. The obtained emission signal ranged from 300 to 950 nm. The background spectrum was eliminated automatically in all recorded spectra. The structural analysis of coatings was performed by X-ray diffraction with Cu Kα radiation using a Bruker D8 diffractometer in Bragg/Brentano mode at 40 mA and 40 kV. The scanning angular (2θ) was ranged from 30 to 60° at a scanning speed of 4°/min. The cross-section scanning electron morphologies and the thickness of coatings were carried out by scanning electron microscope of Netherlands, FEI Quanta 200F. Secondary electron images (SEI) and backscattered electron images (BEI) were used to characterize the overall coatings thickness. Residual stress of the coatings was calculated based on the $\cos^2\Psi\sin^2\Psi$ method, where Ψ is the angle between the normal to the coating surface and the diffracting lattice planes. The X-ray diffraction peak position shifts with the Ψ angle. The formula to calculate the residual stress is [22]:

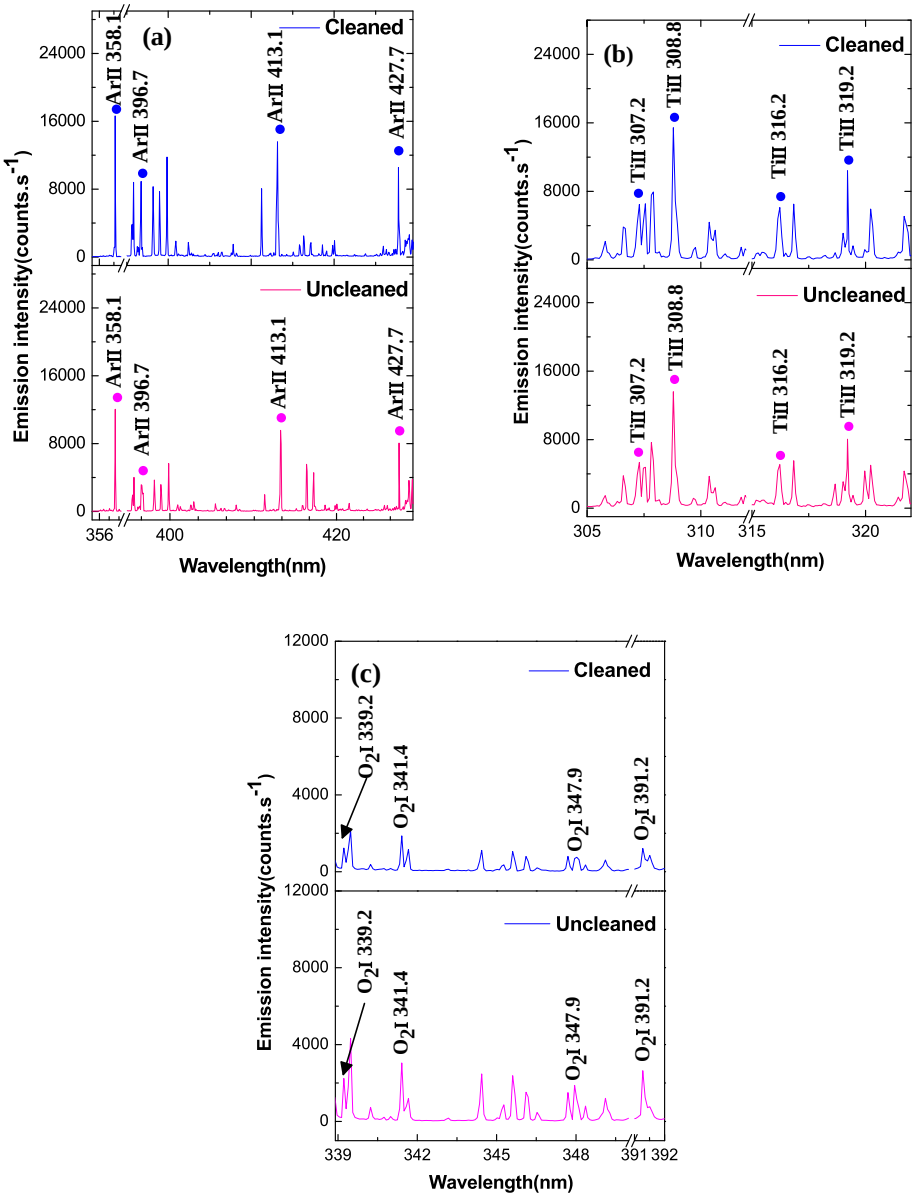

Fig. 3. Spectral intensity of representative ArII, TiII and O_2I at different plasma conditions.

$$(d_{hkl} - d_0)d_0 = \frac{1}{2}S_2 * \sigma * cos^2\alpha * sin^2\Psi + \frac{1}{2}S_2 * \sigma * sin^2\alpha + 2S_1 * \alpha \quad (1)$$

Here, S2 and S1 are coating constants related to the Poisson's ratio and elastic modulus (determined by nanoindentation, different for the coatings with different thickness). α is the angle related to the 2θ diffraction angle and Ψ = 0°, 15°, 20°, 25°, 30°, 35°, 40° and 45°.

The Vicker microhardness was measured by Zwickmicro hardness tester using a pyramidal diamond indenter with an included angle of 136°, 50 g indenting load for 20 s dwell time at 60 μm/s indentation rate. An average of three measurements was taken from five different positions in order to ensure the accuracy and repeatability of hardness. The friction coefficient was measured by ball-on-disk tester at room temperature and relative humidity of 50%. GCr15 ball of 6 mm in diameter with surface roughness Ra of 0.02 mm, 50 g was chosen as the counterpart and 5N load was applied. During the wear test, the relationship between friction coefficient and the sliding time was continuously recorded. The adhesion of the (Ti,AlCr)N coatings was evaluated by Rockwell indentation test using a Rockwell C diamond stylus (cone apex angle 120°, tip radius $R = 0.2$ mm) at an applied load of 150 kg. Surface roughness was measured with an AFM system (Dimension Fastscan, Bruker, USA) at ambient conditions (25 °C, 35–40% Relative Humidity). For every sample the surface roughness (Ra) was inspected by the tapping mode in the areas of 2 × 2 μm^2.

3. Results and discussion

3.1. Surface resistance of chamber wall

Fig. 2 presents the measurement of the surface resistance of the vacuum chamber at several positions. The surface resistance of

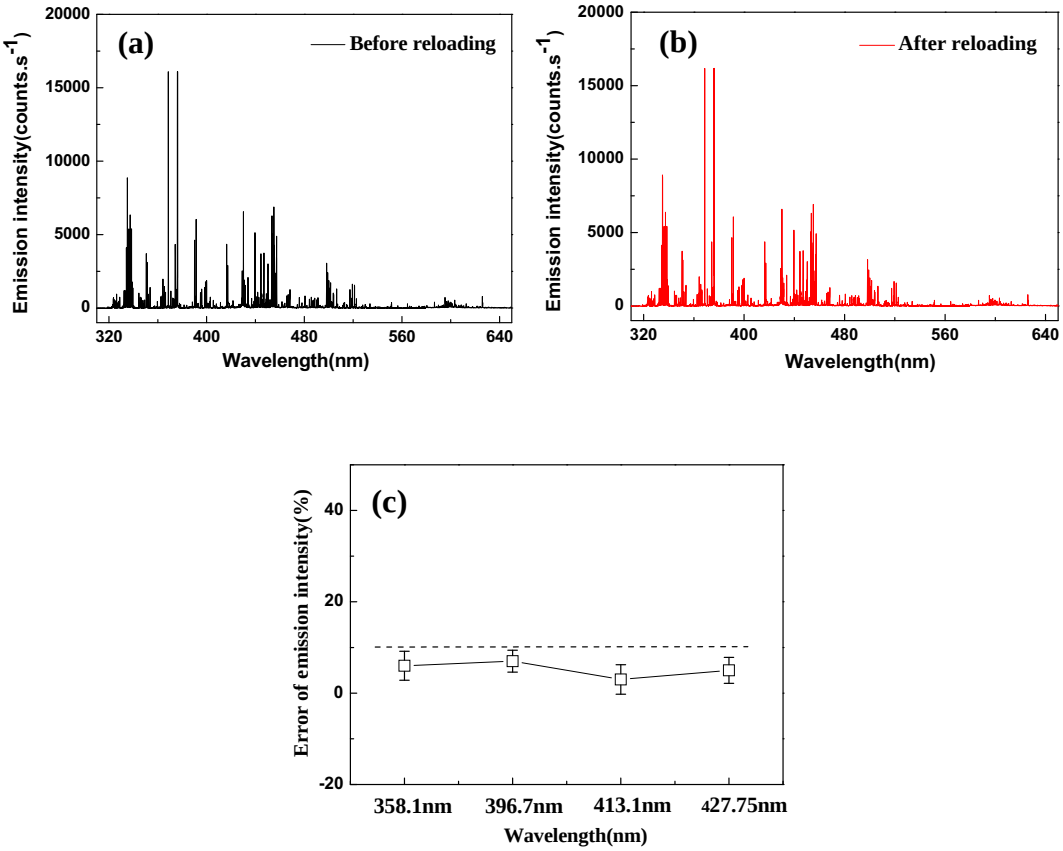

Fig. 4. The error of spectral emission intensity before/after spectrum device was reloaded, (a) Before reloading, (b) After reloading, (c) The error of spectral emission intensity.

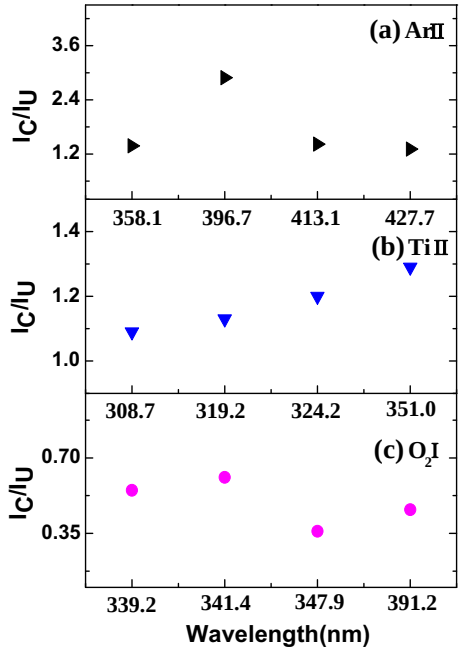

Fig. 5. I_C/I_U ratio of representative ArII, TiII and O_2I at different plasma conditions.

uncleaned chamber was increased by 33.4, 26.8, 403.2, 391.5, 4.3, 8.3, 464.1, 500.8 times than that of cleaned one at the same site: A, B, C, D, E, F, G, H, as indicated in Table 2. It is due to the accumulated sediments on the wall, which affects the equivalent electrical conductivity. Especially in the region on the carousel (e.g, the position E and F), the poor electrical conductivity at uncleaned condition would give rise to the charging effect and the local electric field increased sharply [23], which led to the phenomenon of abnormal charge exchange, even marginal discharge.

Fig. 3 demonstrates the optical emission spectra of ArII, TiIIand O_2I with chamber cleaned or uncleaned. The representative ArII spectra lines (at 358.1, 396.7, 413.1 and 427.7nm), TiII spectra lines (at 307.2, 308.8, 316.2 and 319.2 nm) and O_2I spectra lines (at 435.1, 444.3, 459.6 and 468.2 nm) were recorded. Both the cleaned and uncleaned chamber wall did not change the position of any peak. However, the relative intensity of these peaks was different. It should be pointed that the spectrometer was reloaded for two groups of experiments (cleaned and uncleaned chamber). In order to confirm that the variation of emission intensity was not caused by reloading the instrument, the spectrum was recorded respectively as shown in Fig. 4(a) and (b). The error of spectral emission intensity was less than 10% (Fig. 4(c)) (five measurements were taken to ensure the accuracy and repeatability).

The I_C/I_U ratio of representative ArII, TiII and O_2I is depicted in Fig. 5. Here, I_C and I_U refer to the spectral intensity with the chamber cleaned and uncleaned respectively. The rise in spectra intensity for ArII and TiII with the chamber cleaned was easily observed (Fig. 3(a) and (b)) and the I_C/I_U for ArII and TiII was greater than 1. The population of ArII and TiII was related to the ionization of Ar atoms and Ti atoms in the discharge system. This implies the increase of ionization rate of the Ar and Ti [24]. On the contrary, the spectra intensity of O_2I decreased and the I_C/I_U for O_2I was less than 1, indicating the smaller number of oxygen atom/ions obtained from the clean chamber wall.

Oxygen may be attributed to the water and oxygen gas trapped in the chamber wall. The wall was deposited and contaminated by the plasma and neutrals from the vacuum arc and work gas. A loose and

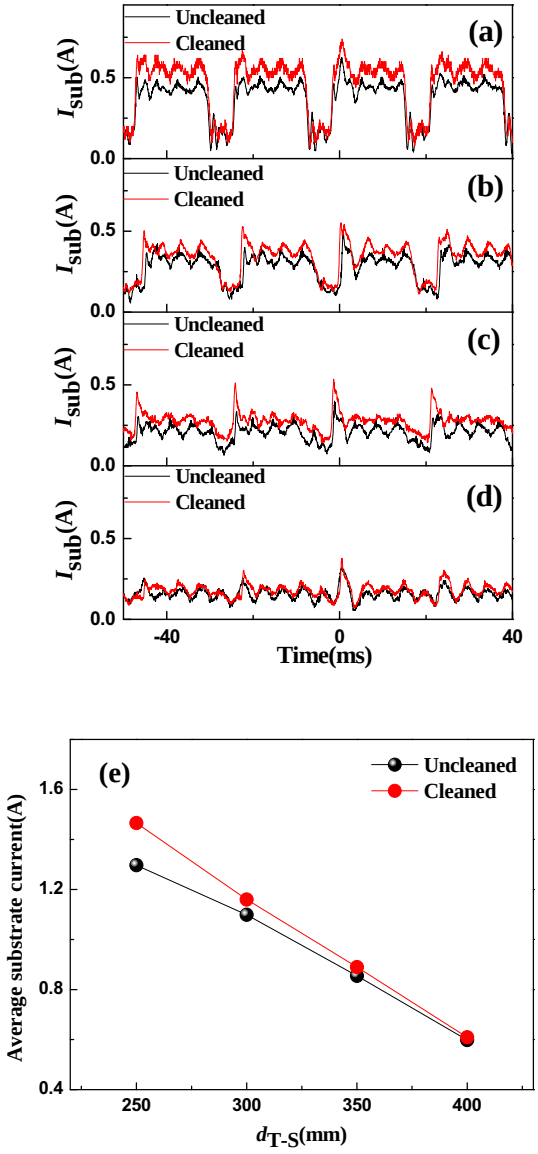

Fig. 6. Substrate current with different plasma conditions: (a) $d_{T\text{-}S}$ = 250 mm, (b) $d_{T\text{-}S}$ = 300 mm, (c) $d_{T\text{-}S}$ = 350 mm, (d) $d_{T\text{-}S}$ = 400 mm, (e) average substrate current.

thick contamination layer (particle, dust, etc.) may be formed on the chamber wall if the coating was deposited without cleaning the wall for a while. The water and oxygen in the air may be trapped in the contamination layer once the chamber door was open to unload or load the components to be treated. When the wall was heated and excited by the energetic particles including ions, electrons and some neutrals, the water and oxygen released and some of them may be excited and ionized by electrons. Thus the oxygen spectral emission intensity was high in the uncleaned chamber than in the cleaned chamber, which implied much richer residual oxygen.

Fig. 6 depicts the substrate current with the chamber cleaned and uncleaned. The average substrate current with cleaned chamber was increased by 13.0%, 5.6%, 4.1% and 1.9% with constant $d_{T\text{-}S}$ respectively. According to Child-Langmuir law ($J_i \propto n_0^{\frac{2}{3}}$, where J_i is ion current, n_0 is plasma density [25,26]), a higher plasma density would lead to a larger ion current. As shown in Fig. 3, a cleaned chamber produced higher plasma density and a higher current was achieved. It may produce a determinate effect on microstructure and surface properties of coatings [27].

As illustrated in Fig. 7, with the cleaned chamber condition, the resistance of chamber was equal to zero ($R_1 = 0$). In contrast, the equivalent resistance induced by contamination layer deposited on chamber wall was not zero with the chamber uncleaned (Fig. 7(a)). According to Ohm's law applied in the arc [28]:

$$U_f = U_{R0} + U_{R1} + U_a \tag{2}$$

$$I_{arc} = \frac{U_f}{R_0 + R_1 + R_{arc}} = \frac{Ua}{R_{arc}} \tag{3}$$

(where U_f is the constant voltage of the power source, U_a is the voltage across the arc, U_{R0} is the voltage across the internal resistance of power source, U_{R1} is the voltage across the contamination layer of chamber wall, R_0 is the internal resistance of power source, R_{arc} is the arc resistance, R_1 is the resistance of chamber wall, and I_{arc} is the current flowing through the entire circuit). The maximum output current of the power supply was determined by Eq. (3):

$$I_{max} = \frac{U_f}{R_0 + R_1} \tag{4}$$

when the chamber was cleaned inferring that R_1 was equal to zero, the maximum current was equal to $I_{max1} = U_f / R_0$ and external characteristics of the power supply corresponded to the curve 1. The curve 2 represented the external characteristics of the power supply with the chamber uncleaned ($R_1 \neq 0$). And the maximum current was equal to $I_{max2} = U_f / (R_0 + R_1)$.

The power supply ran at constant current mode. With the chamber uncleaned, the resistance of the contamination layer (R_1) gave rise to a low equivalent arc voltage (U_{a2}) compared to original arc voltage (U_{a1}). The arc ran at a slightly lower voltage since the resistance of R_1 is not significant. This led to a lower input power to the arc system. Consequently the discharge was weakened and plasma density became lower as shown in Fig. 3. A reduced substrate current was observed (Fig. 6), which was not beneficial for the densification of deposited coatings.

3.2. Microstructure and properties of (Ti,AlCr)N coatings

Fig. 8 illustrates the X-ray diffractograms of the (Ti,AlCr)N coatings. As expected, the crystalline microstructure matches with the NaCl-B1 type structure (FCC) of aluminum chromium nitride and titanium nitride (JCPDS card #00-046-1200 and # 01-070-2942). For each scan, the change of diffraction intensity of cubic(*c*-) AlCrN (200) peak was neglected. However, the diffraction intensity of cubic(*c*-) AlCrN (111) peak increased distinctly with the chamber cleaned. The (Ti,AlCr)N coatings deposited with the chamber uncleaned (hereinafter referred to as U-(Ti,AlCr)N coatings) possessed lower crystallinity as indicated by the lower intensity. The lower mobility of adatoms on the surface, due to the less ion bombardment indicated by smaller substrate current (Fig. 6), would translate into weak crystallization and insufficient coalescence of grains and islands [29].

With the chamber cleaned, arc discharge was enhanced and plasma density was higher near the substrate. Thus a larger substrate current was achieved. The intensive ion bombardment gave rise to the distortion of crystal lattice and the shift of diffraction peaks. A shift of diffraction peak to lower angles was related to the internal stress in the coatings [30]. According to Bragg equation, $1 / dhkl = (2/\lambda) \sin\theta$,

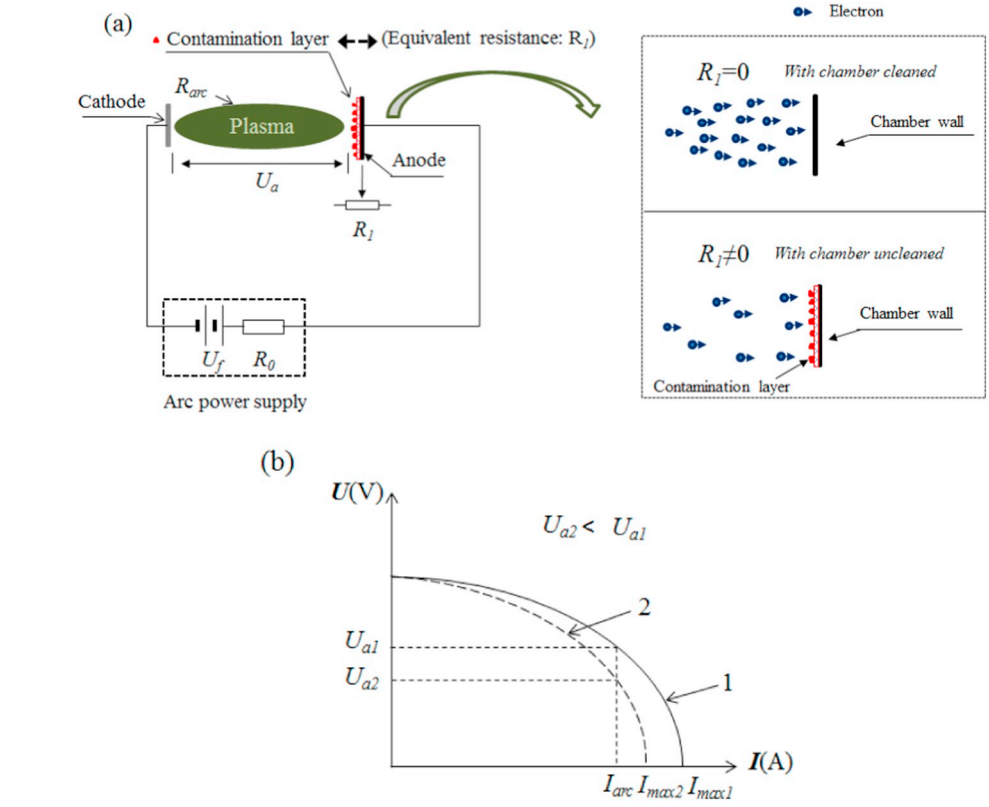

Fig. 7. Equivalent illustration of different discharge conditions:
(a) Different chamber conditions, (b) external characteristic curve of arc power supply.

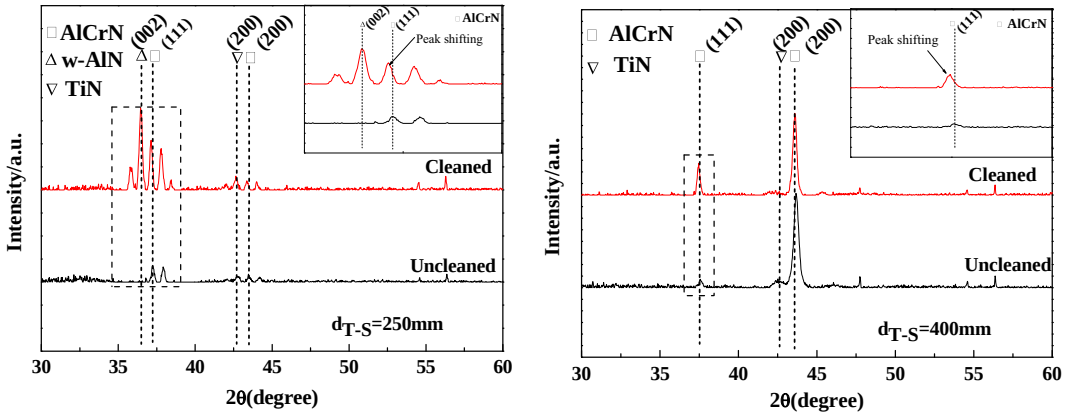

Fig. 8. X-ray diffraction patterns of the (Ti,AlCr)N coatings.

Table 3
Residual stress of coatings with different chamber wall conditions.

Condition	Residual stress (GPa)			
	d_{T-S} = 250(mm)	d_{T-S} = 300(mm)	d_{T-S} = 350(mm)	d_{T-S} = 400(mm)
Uncleaned	−4.41	−4.13	−3.67	−3.19
Cleaned	−4.74	−4.32	−3.75	−3.24

where dhkl, λ, and θ are the interplanar spacing of the (hkl) plane, wavelength of the X-ray, and half of the diffraction angle, respectively. The *d* value became larger when diffraction angle slightly shifted to the left. Table 3 demonstrates the residual stress of coatings with different chamber wall conditions. The compressive stress of C-(Ti,AlCr)N coatings was slightly larger than that of U-(Ti,AlCr)N coatings. It was attributed to the effect of atomic peening resulting from more ion bombardment, which may contribute to enhancement of mechanical

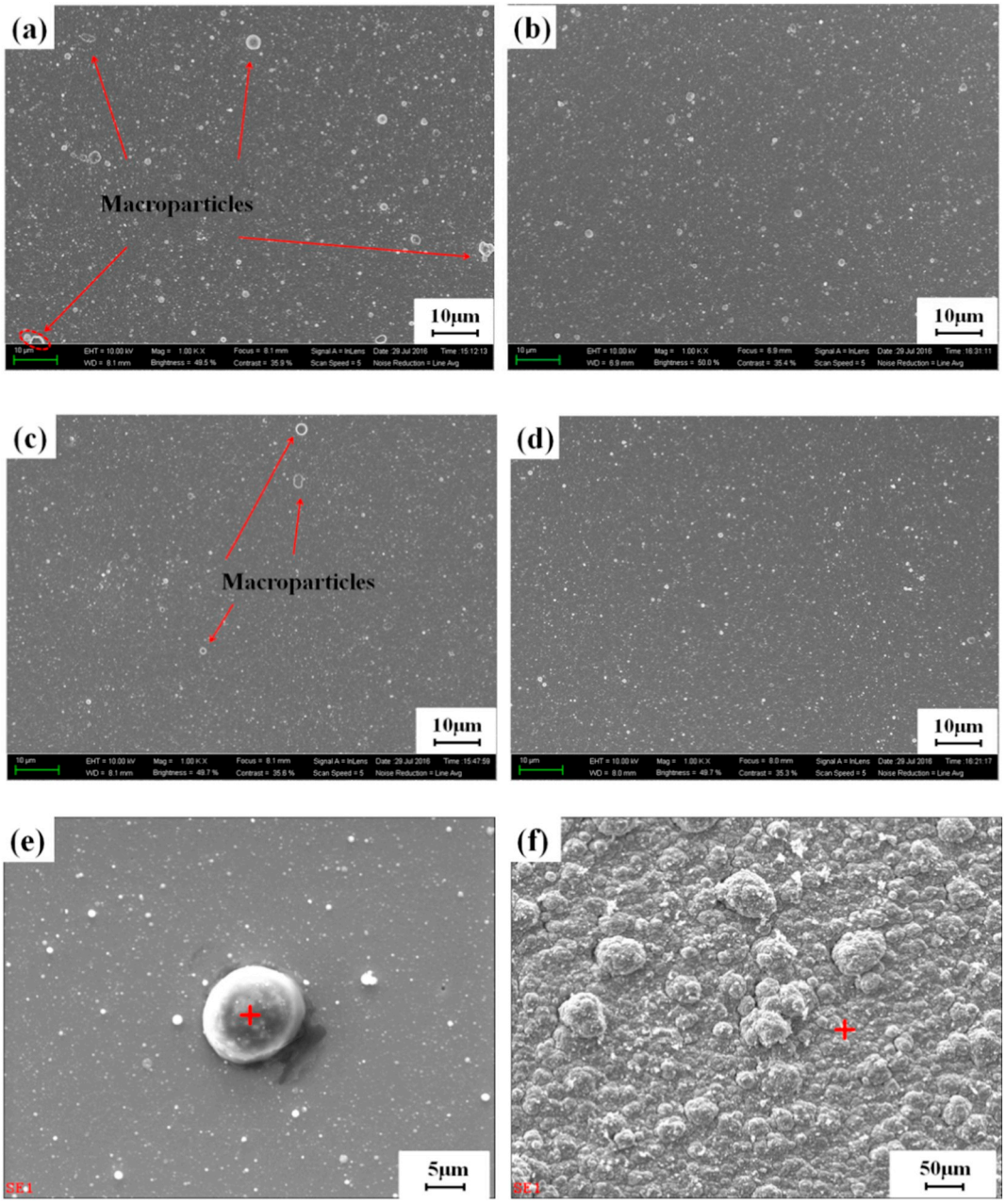

Fig. 9. Surface micrograph of the coatings deposited at different conditions: (a) U-$d_{T\text{-}S}$ = 250 mm, (b) C-$d_{T\text{-}S}$ = 250 mm, (c) U-$d_{T\text{-}S}$ = 400 mm, (d) C-$d_{T\text{-}S}$ = 400 mm. (U-$d_{T\text{-}S}$ and C-$d_{T\text{-}S}$ refer to the Uncleaned-$d_{T\text{-}S}$ and Cleaned-$d_{T\text{-}S}$), (e) surface macroparticle, (f) the contamination layer on the chamber wall.

Table 4
Elemental composition (by EDS) of coatings deposited with different conditions (in Fig. 9(a), (b, (c) and (d)), and the composition of surface macroparticle and the contamination layer on the chamber wall (in Fig. 9(e) and (f)).

	Composition (wt%)			
	Ti	Al	Cr	N
U-$d_{T\text{-}S}$ = 250 mm	46.73	19.78	25.71	7.78
C-$d_{T\text{-}S}$ = 250 mm	47.01	18.27	26.51	8.21
U-$d_{T\text{-}S}$ = 400 mm	46.02	19.84	26.28	7.86
C-$d_{T\text{-}S}$ = 400 mm	45.95	19.63	25.92	8.50
Macroparticle	58.32	15.86	21.35	4.46
Contamination layer	48.74	20.97	21.45	8.84

properties to some extent.

Fig. 9 shows the surface morphology of the (Ti,AlCr)N coatings. Larger size macroparticles were observed prominently on the surface of U-(Ti,AlCr)N coatings, whereas, the number of the defects decreased evidently on the surface of (Ti,AlCr)N coatings with the chamber cleaned (hereinafter referred to as C-(Ti,AlCr)N coatings). Table 4 presents the elemental composition of the some macroparticles on the deposited surface and the contamination layer on the chamber wall in Fig. 9(e) and (f). They had the same elements (including Ti,Al,Cr and N) although the concentration was slightly different. Especially more defects were observed with the chamber uncleaned, inferring they may originate from cathodic arc as well as dirty chamber wall [31]. These particles and contaminations easily broke away due to the mechanical micro-vibration, the collision between electrons, energetic neutrals and

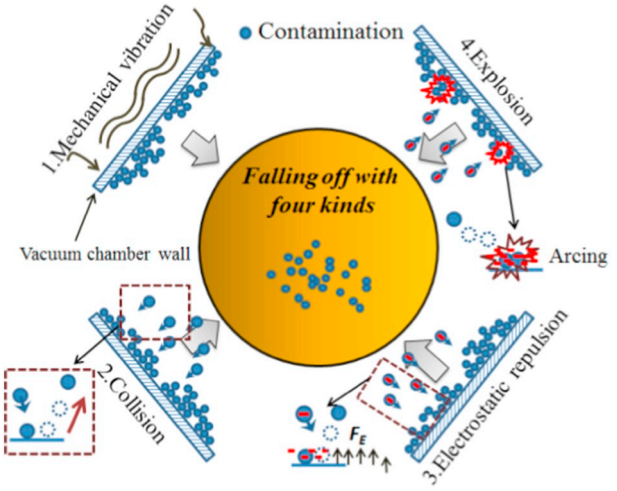

Fig. 10. Illustration of peeling off of contaminations from chamber wall.

chamber wall as illustrated in Fig. 10. Besides, the poor electrical conductivity of chamber wall (Table 2) might result in the charging effect, electrostatic repulsion and even local micro-arc, which produced more peeling off of contaminations. The macroparticles from the wall floated in the chamber in conjunction with those from the cathodic arc. The contaminations were loosely adhered on the surface due to the weakened bombardment effect with chamber uncleaned.

These particles may be charged with electrons, which were repelled far from substrate surface when the negative bias is applied [32–34]. And intensive ion bombardment tended to get rid of the macroparticles on the surface [35–37]. With the chamber cleaned a higher plasma

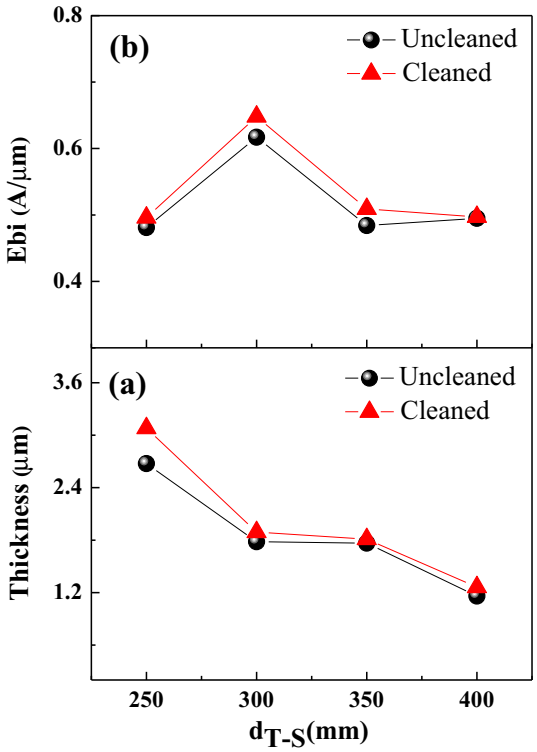

Fig. 12. Thickness of coatings D, and E_{bi} at different conditions: (a) Coating thickness D, (b) E_{bi}.

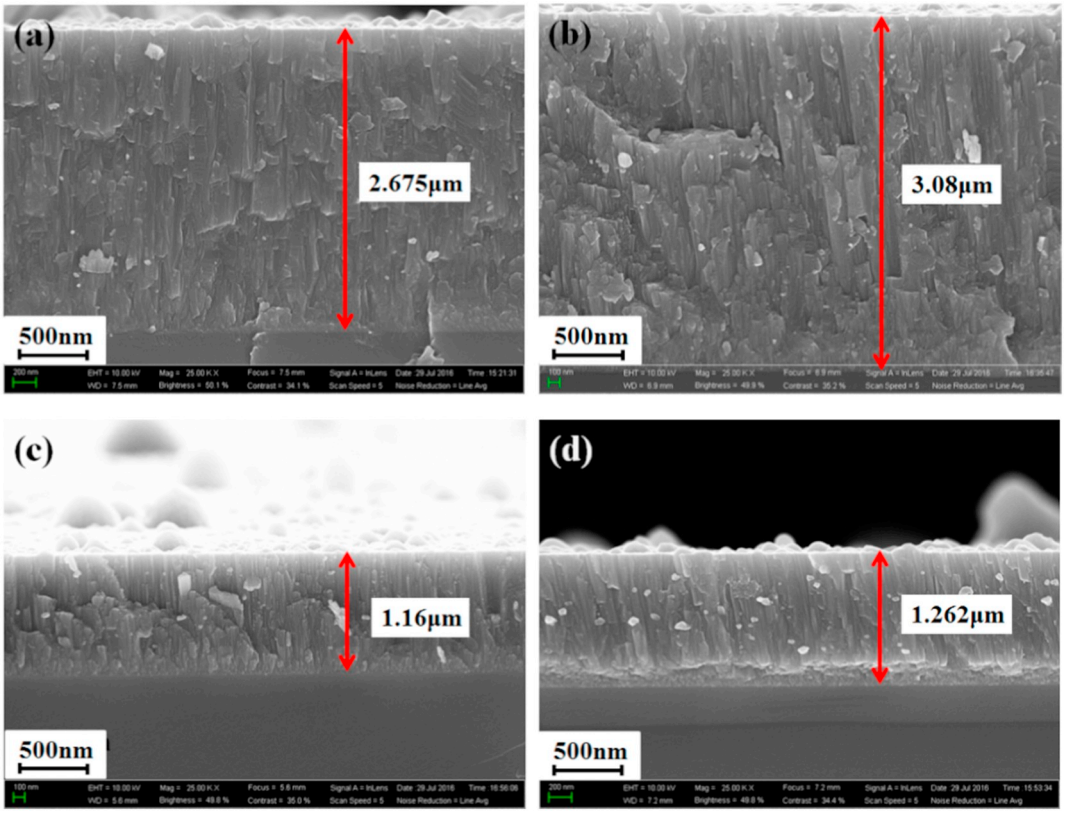

Fig. 11. Cross-sectional morphology of the coatings deposited at different conditions: (a) U-$d_{T\text{-}S}$ = 250 mm, (b) C-$d_{T\text{-}S}$ = 250 mm, (c) U-$d_{T\text{-}S}$ = 400 mm, (d) C-$d_{T\text{-}S}$ = 400 mm.

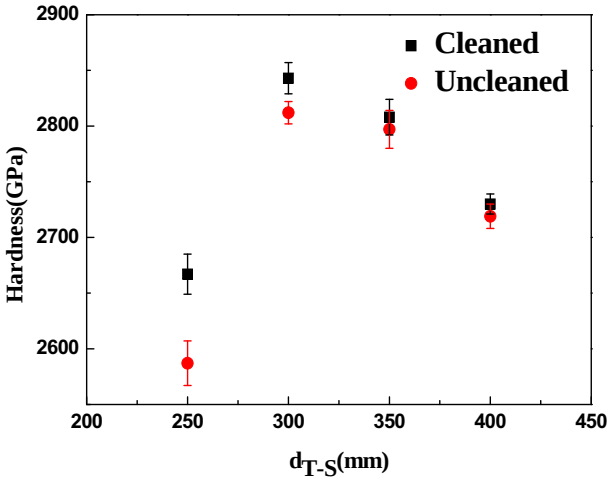

Fig. 13. Microhardness of the (Ti,AlCr)N coatings.

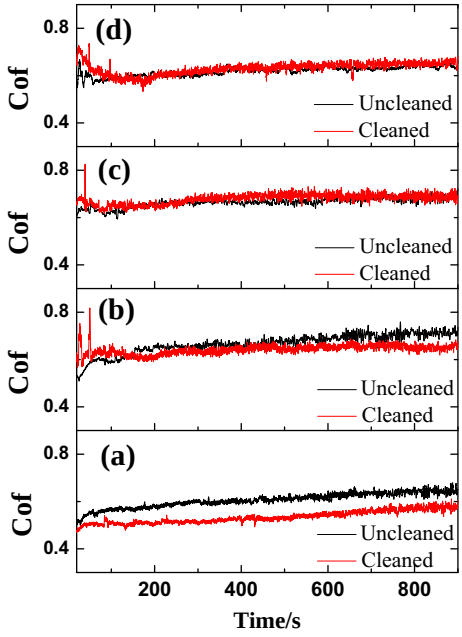

Fig. 14. Friction coefficients of the (Ti,AlCr)N coatings at different conditions: (a)250 mm, (b)300 mm, (c)350 mm, (d)400 mm.

Table 5
Roughness of coatings with different chamber wall conditions.

Condition	Ra(nm)			
	$d_{T\text{-}S}$ = 250 mm	$d_{T\text{-}S}$ = 300 mm	$d_{T\text{-}S}$ = 350 mm	$d_{T\text{-}S}$ = 400 mm
Uncleaned	88.3	71.8	63.4	52.6
Cleaned	86.7	67.4	62.6	52.3

density gave rise to more effect of repelling and bombardment to the macroparticles. Consequently fewer defects were observed on the surface compared to those with the chamber uncleaned, due to synergistic effect of less contamination and higher plasma density.

Fig. 11 demonstrates the cross-sectional micrographs of (Ti,AlCr)N coatings deposited. All of coatings presented the compact structures with columnar growth. The C-(Ti,AlCr)N coatings have a higher deposition rate as shown in Fig. 12(a). As mentioned in Fig. 6, the substrate ion current increased after the chamber is cleaned. A higher more ionic flux exerted a positive effect on the higher deposition rate. In fact the high density plasma may be also related to a larger input power to cathodic arc. A slight increase of arc voltage was induced as illustrated in Fig. 7. This led to more evaporation of target materials. An increased deposition rate was achieved due to high density of ions and atoms.

Fig. 12 summaries the changes in the coating thickness (D) and E_{bi} as a function of target-substrate distance. The E_{bi} refers to the ratio of substrate ion current to thickness, which is frequently used to evaluate the compactness of the coating [38]. The substrate current is proportional to the number of incident ions depending on plasma density around samples. A larger E_{bi} value implies that the coating may be bombarded by more energetic ions and denser film may be produced. As depicted in Fig. 12(b), the cleaned chamber gave rise to an increased E_{bi}, suggesting that the more compact structure of C-(Ti,AlCr)N coatings was induced although the deposition rate increased evidently.

Fig. 13 exhibits the vickers micro-hardness of the (Ti,AlCr)N coatings. The C-(Ti,AlCr)N coatings has a relatively higher hardness compared to U-(Ti,AlCr)N coatings with the same $d_{T\text{-}S}$. It may be attributed to several factors. A higher hardness is related to larger residual stress [39–40] of C-(Ti,AlCr)N coatings, which is supported by XRD results as shown in Fig. 8. Another hardening factor is densification effect of micro-structure [41]. More blocks are allowed to create at grain boundaries, thus inducing the pinning effect, inhibiting the migration and strengthening the influence of dislocation blocking against the grain boundary [42]. The E_{bi} value of C-(Ti,AlCr)N coatings (Fig. 12) increases to some extent, which indicates that the densification of coatings is improved than that of the U-(Ti,AlCr)N coatings. Therefore, the C-(Ti,AlCr)N coatings hardness is enhanced dramatically. Besides, the growth of C-(Ti,AlCr)N coatings demonstrates a stronger diffraction intensity of c-(111) plane (Fig. 8). The effect of the coherency strain (c-plane) may contribute to enhancement of hardness [43]. At the $d_{T\text{-}S}$ of 250 mm, the hardness of C-(Ti,AlCr)N coating was evidently higher than that of U-(Ti,AlCr)N coating. It may be attributed to the superlattice effect [44], indicated by “the satellite shaped diffraction peaks” as shown in Fig. 8. An alternating stress field was induced and the crystal boundary energy was increased, which could restrict the motion of dislocations and enhance the hardness of the coating [45]. Moreover, with the chamber cleaned, the fewer macroparticles would slightly interfere the dislocation arrays and the coupling effect between sharp interfaces is well strengthened [46], which results in an increase of hardness. As the $d_{T\text{-}S}$ increases, the difference of hardness of (Ti,AlCr)N coatings with the chamber cleaned or uncleaned was unconspicuous. It may be attributed to the similar E_{bi}.

Fig. 14 shows the friction coefficient (COF) of the (Ti,AlCr)N coatings. The gradual evolution of COF was detected during the full test. The friction behavior of each sample underwent a pre-grinding stage about 200 s, which was quite complex and mainly related to the surface conditions. Then the coefficients were approximately kept stable for the rest of whole sliding time. The COF of U-(Ti,AlCr)N coatings was slightly larger than that of C-(Ti,AlCr)N coatings, which can be associated with the roughness of surface [47,48]. Table 5 illustrates the roughness (Ra) of the produced coatings. The Ra values of U-(Ti,AlCr)N coatings was slightly larger than that of C-(Ti,AlCr)N coatings, which was related to the existence of more macroparticles (Fig. 9) on the surface of U-(Ti,AlCr)N coatings. Higher roughness reduced the actual contact area between the ball and coating, which resulted in the load only focusing on the contact areas and then enhanced the friction

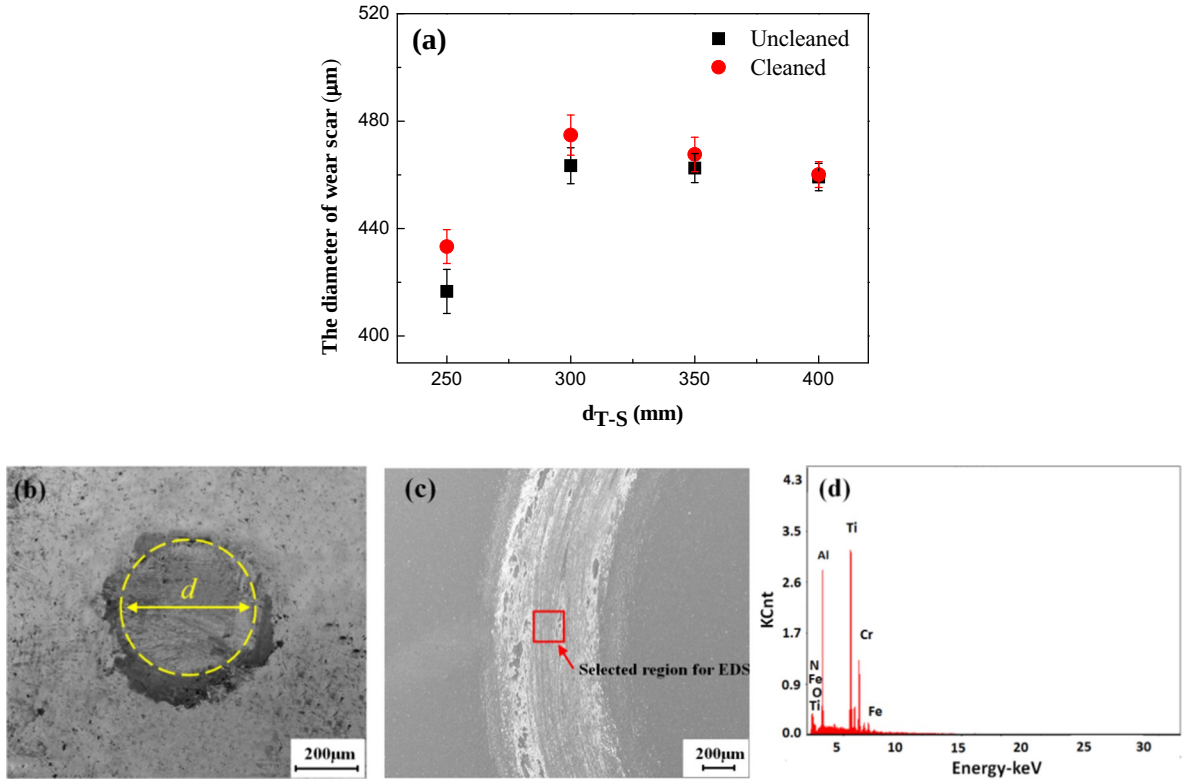

Fig. 15. The size and typical SEM image of wear surface, (a) the diameter of wear scar on the ball, (b) typical SEM image of wear scar, (c) micrograph of wear-track surface, (d) EDS elemental composition of the wear-track surface.

Table 6
EDS elemental composition of the wear track surfaces with different coatings.

Condition	d_{T-S}	Element (at. %)					
		Ti	Al	Cr	N	O	Fe
Uncleaned	250 mm	34.24	21.89	17.05	14.77	10.41	02.04
	300 mm	31.32	15.96	15.79	02.33	24.59	10.01
	350 mm	33.12	15.48	18.59	03.30	22.01	07.50
	400 mm	34.59	19.55	18.30	15.02	07.13	05.41
Cleaned	250 mm	31.13	20.99	17.52	12.66	13.83	03.87
	300 mm	31.91	15.28	12.33	02.33	25.75	12.40
	350 mm	32.08	16.29	16.31	03.29	23.35	08.69
	400 mm	33.65	19.11	18.08	15.12	08.59	05.45

coefficient of the coating [49]. In addition, the decreased substrate current of U-(Ti,AlCr)N coatings implied weak bombardment effect leading to less compactness of the coatings.

Fig. 15(a) and (b) show the wear of the friction counterparts. The diameter of wear scar of the ball against C-(Ti,AlCr)N coatings was larger than that against U-(Ti,AlCr)N coatings. The ball sliding on harder coating exhibited larger wear area demonstrating higher wear rate [50]. When sliding, the harder coatings (C-(Ti,AlCr)N) could lead to a considerable wear volume of the balls. Fig. 15(c) and (d) present the typical image and EDS elemental analysis of wear track surface. Table 6 presents the elements in the wear track surfaces of different coatings. The Fe element was detected on the coatings (which were not broken through at a closer look. In addition, no violent fluctuations of friction coefficient were found (Fig. 14)), indicating that the debris was related to the counterpart balls [51]. In fact the temperature at the interface between the ball and coatings was elevated during the sliding process, which would cause oxidation [52] (Oxygen was detected on worn surfaces as shown in Table 6). The content of Fe (at. %) on the wear track surface of U-(Ti,AlCr)N coatings is slightly lower than that on C-(Ti,AlCr)N coatings. For the steel ball, the debris was generated on the nitride coating, which could be entrapped into the rubbing surface, resulting in the formation of scratch and consequently the wear mechanism was mainly abrasive wear [53]. In abrasion wear, the steel ball and the coating surface would rub each other resulting in plastic deformation, flow and microcutting, etc. Additionally, the iron oxide layer from steel ball also adhered to the coating surface due to higher hardness of nitride [54]. With the chamber cleaned, the hardness of C-(Ti,AlCr)N coating was enhanced, inducing more materials from counterpart ball were abraded down and a higher Fe concentration was found on the wear track surface of coating.

Fig. 16 depicts the surface morphology of samples after indentation by using TH320 Rockwell hardness tester (load of 1470N). In reference to standard drawing VDI 3198 (the standard damage pictures serve to classify adhesion into six classes HF1-HF6 [55]), the adhesion strength between the C-(Ti,AlCr)N coatings and substrate was relatively high. The spallation of U-(Ti,AlCr)N coating at d_{T-S} = 250 mm was observed clearly and the adhesion strength seemed to be the poorest, which can be identified as class HF5. The C-(Ti,AlCr)N coating at d_{T-S} = 250 mm showed only a few cracks around the indentation referred to as class HF2. The poor adhesion of coatings may be attributed to a higher stress stemming from larger thickness and excessively intensive bombardment. In contrast, the indentation for the C-(Ti,AlCr)N coating at d_{T-S} = 300 mm was clear and smooth with no spherical cracks and dew points. The adhesion may be identified as HF1, which is distinctly superior to that of U-(Ti,AlCr)N coating.

With the chamber cleaned, less water and oxygen trapped in the contamination layer would release and be excited and/or ionized as shown in Fig. 3. A better interface is expected. A cleaned chamber may lead to a higher plasma density and an effective ion-sputtering of native oxides and impurities, which gives rise to an increase in the coating

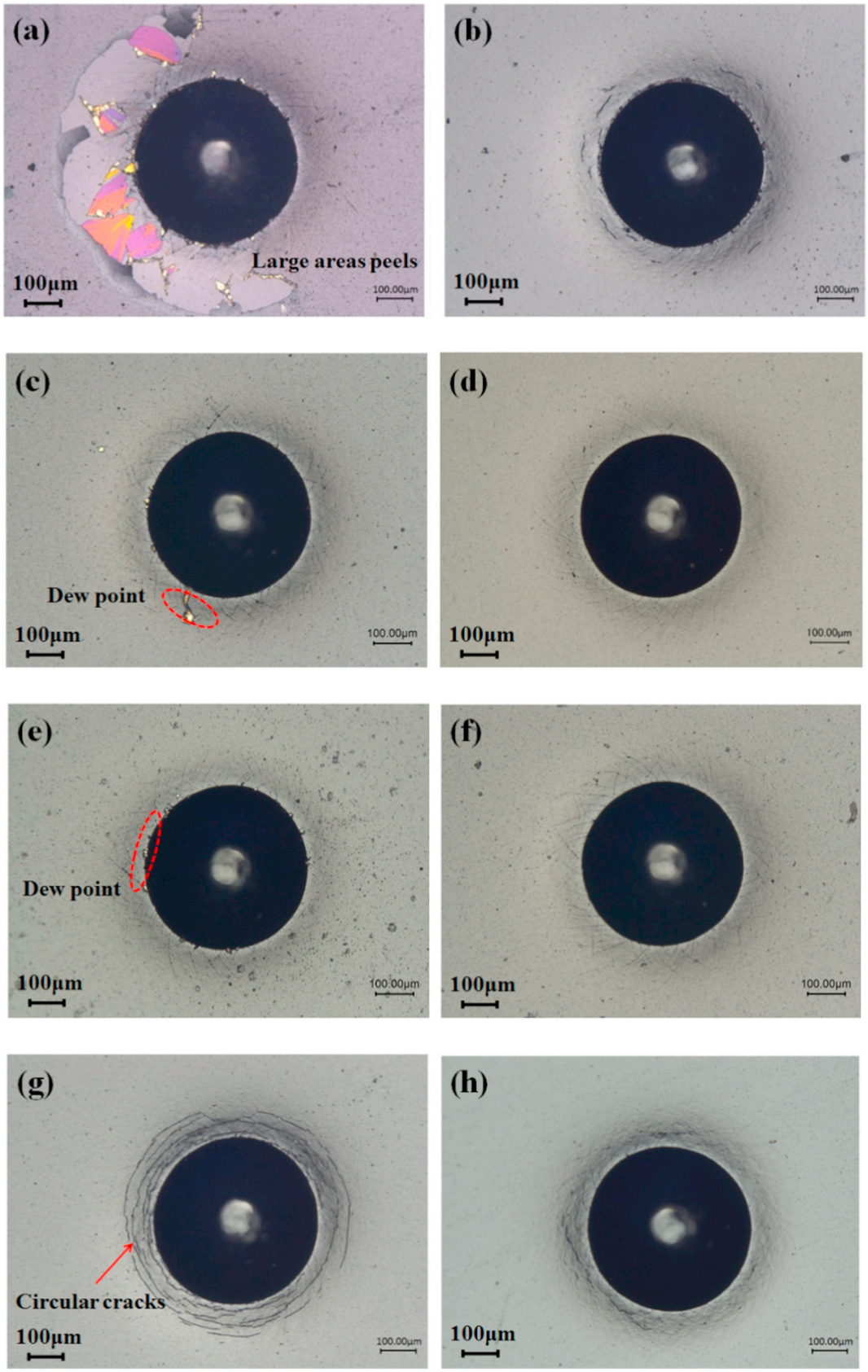

Fig. 16. The indentation morphology of the (Ti,AlCr)N coatings at different conditions:
(a) U-$d_{T\text{-}S}$ = 250 mm, (b) C-$d_{T\text{-}S}$ = 250 mm, (c) U-$d_{T\text{-}S}$ = 300 mm, (d) C-$d_{T\text{-}S}$ = 300 mm, (e) U-$d_{T\text{-}S}$ = 350 mm, (f) C-$d_{T\text{-}S}$ = 350 mm, (g) U-$d_{T\text{-}S}$ = 400 mm, (h) C-$d_{T\text{-}S}$ = 400 mm.

adhesion [56]. Grain refinement induced by intensive ion bombardment may increase crack propagation resistance [57], which could restrain the coating peeling.

4. Conclusion

The (Ti,AlCr)N coatings have been deposited by the cathodic arc technique with the chamber cleaned and uncleaned. The chamber cleaning has a distinct effect on the substrate ion current, plasma emission spectrum, microstructure, surface defects and mechanical properties of coatings. With the chamber cleaned, the equivalent resistance of chamber wall was significantly reduced. The higher emission spectrum intensity of ArII confirmed an enhanced arc discharge and low emission intensity of O_2I indicated the reduced content of residual oxygen. Less surface defects on the surface of C-(Ti,AlCr)N coatings were observed and the thickness of coatings was increased by 15.1%. Besides, higher substrate current with larger E_{bi} value was achieved inferring the increased densification of films. The mechanical properties of C-(Ti,AlCr)N coatings were improved with elevated hardness, decreased friction coefficient and optimized adhesion between the film and substrate (HF1). Accordingly, in coating practices, the monitoring and cleaning of chamber wall is critical.

Acknowledgements

The authors acknowledge financial support from Natural Science Foundation of China (No. 11675047, 11875119, 51811530059), and State Key Laboratory of Advanced Welding and Joining, Harbin Institute of Technology (AWPT-Z02).

References

[1] L. Chen, Y.X. Xu, L.J. Zhang, Influence of TiN and ZrN insertion layers on the microstructure, mechanical and thermal properties of Cr-Al-N coatings, Surf. Coat. Technol. 285 (2016) 146–152.
[2] L. He, L. Chen, Y. Xu, Interfacial structure, mechanical properties and thermal stability of CrAlSiN/CrAlN multilayer coatings, Mater. Charact. 125 (2017) 1–6.
[3] L. Chen, Y. Du, P.H. Mayrhofer, S.Q. Wang, J. Li, The influence of age-hardening on turning and milling performance of Ti-Al-N coated inserts, Surf. Coat. Technol. 202 (2008) 5158–5161.
[4] J. Lin, B. Mishra, J.J. Moore, W.D. Sproul, A study of the oxidation behavior of CrN and CrAlN thin films in air using DSC and TGA analyses, Surf. Coat. Technol. 202 (2008) 3272–3283.
[5] H.C. Barshilia, N. Selvakumar, B. Deepthi, K.S. Rajam, A comparative study of reactive direct current magnetron sputtered CrAlN and CrN coatings, Surf. Coat. Technol. 201 (2006) 2193–2201.
[6] C.B. Liu, W. Pei, F. Huang, L. Chen, Improved mechanical and thermal properties of CrAlN coatings by Si solid solution, Vacuum 125 (2016) 180–184.
[7] G.S. Fox-Rabinovich, A.I. Kovalev, M.H. Aguirre, B.D. Beake, K. Yamamoto, S.C. Veldhuis, J.L. Endrino, D.L. Wainstein, A.Y. Rashkovskiy, Design and performance of AlTiN and TiAlCrN PVD coatings for machining of hard to cut materials, Surf. Coat. Technol. 204 (2009) 489–496.
[8] K. Yamamoto, T. Sato, K. Takahara, K. Hanaguri, Properties of (Ti,Cr,Al)N coatings with high Al content deposited by new plasma enhanced arc-cathode, Surf. Coat. Technol. 174 (2003) 620–626.
[9] J. Ramm, M. Ante, T. Bachmann, B. Widrig, H. Brändle, M. Döbeli, Pulse enhanced electron emission (P3e™) arc evaporation and the synthesis of wear resistant Al-Cr-O coatings in corundum structure, Surf. Coat. Technol. 202 (2007) 876–883.
[10] J. Ramm, M. Ante, H. Brändle, A. Neels, A. Dommann, M. Döbeli, Thermal stability of thin film corundum-type solid solutions of $(Al_{1-x}Cr_x)_2O_3$ synthesized under low temperature non-equilibrium conditions, Adv. Eng. Mater. 9 (2007) 604–608.
[11] B. Warcholinski, A. Gilewicz, Effect of substrate bias voltage on the properties of CrCN and CrN coatings deposited by cathodic arc evaporation, Vacuum 90 (2013) 145–150.
[12] W. Liu, A. Li, H. Wu, Y. Long, J. Huang, X. Deng, C. Wang, Q. Wang, S. Wu, Effects of gas pressure on microstructure and performance of (Ti, Al, Zr)N coatings produced by physical vapor deposition, Ceram. Int. 42 (2016) 17436–17441.
[13] R.F. Londoño-Menjura, R. Ospina, D. Escobar, J.H. Quintero, J.J. Olaya, A. Mello, E. Restrepo-Parra, Influence of deposition temperature on WTiN coatings tribological performance, Appl. Surf. Sci. 427 (2017) 1096–1104.
[14] A.W. Zia, Z. Zhou, P.W. Shum, L.K.Y. Li, The effect of two-step heat treatment on hardness, fracture toughness, and wear of different biased diamond-like carbon coatings, Surf. Coat. Technol. 320 (2017) 118–125.
[15] S. Zhang, H. Xie, Improving the adhesion of amorphous carbon coatings on cemented carbide through plasma cleaning, Surf. Coat. Technol. 113 (1999) 120–125.
[16] C.W.M.E. Silva, E. Alves, A.R. Ramos, C.S. Sandu, A. Cavaleiro, Adhesion failures on hard coatings induced by interface anomalies, Vacuum 83 (2009) 1213–1217.
[17] H. Tanoue, M. Kamiya, S. Oke, Y. Suda, H. Takikawa, Y. Hasegawa, M. Taki, N. Tsuji, T. Ishikawa, H. Yasui, S. Temmei, H. Takahashi, Effect of gas introduction position on substrate etching by means of Ar-dominated graphite-cathodic-arc plasma beam in μT-FAD, Thin Solid Films 518 (2010) 3546–3550.
[18] M. Hans, M. Baben, Y.T. Chen, K.G. Pradeep, D.M. Holzapfel, D. Primetzhofer, D. Kurapov, J. Ramm, M. Arndt, H. Rudigier, J.M. Schneider, Substrate rotation-induced chemical modulation in Ti-Al-O-N coatings synthesized by cathodic arc in an industrial deposition plant, Surf. Coat. Technol. 305 (2016) 249–253.
[19] Y. Long, A. Javed, I. Shapiro, Z.K. Chen, X. Xiong, P. Xiao, The effect of substrate position on the microstructure and mechanical properties of SiC coatings on carbon/carbon composites, Surf. Coat. Technol. 206 (2011) 568–574.
[20] K.D. Bouzakis, E. Bouzakis, G. Skordaris, S. Makrimallakis, A. Tsouknidas, G. Katirtzoglou, S. Gerardis, Effect of PVD films wet micro-blasting by various Al_2O_3 grain sizes on the wear behaviour of coated tools, Surf. Coat. Technol. 205 (2011) S128–S132.
[21] S. Tanaka, T. Shirochi, H. Nishizawa, K. Metoki, H. Miura, H. Hara, T. Takahashi, Micro-blasting effect on fracture resistance of PVD-AlTiN coated cemented carbide cutting tools, Surf. Coat. Technol. 308 (2016) 337–340.
[22] C.H. Ma, J.H. Huang, H. Chen, Residual stress measurement in textured thin film by grazing-incidence X-ray diffraction, Thin Solid Films 418 (2002) 73–78.
[23] G. Erkens, R. Cremer, T. Hamoudi, K.D. Bouzakis, I. Mirisidis, S. Hadjiyiannis, G. Skordaris, A. Asimakopoulos, S. Kombogiannis, J. Anastopoulos, K. Efstathiou, Properties and performance of high aluminum containing (Ti,Al)N based super-nitride coatings in innovative cutting applications, Surf. Coat. Technol. 177 (2004) 727–734.
[24] J.T. Gudmundsson, Ionization mechanism in the high power impulse magnetron sputtering (HiPIMS) discharge, J. Phys. Conf. Ser. 100 (2008) 082013–082016.
[25] I. Langmuir, The effect of space charge and initial velocities on the potential distribution and thermionic current between parallel plane electrodes, Phys. Rev. 21 (1923) 419–435.
[26] X. Tian, P.K. Chu, Modeling of the relationship between implantation parameters and implantation, Phys. Lett. A 277 (2000) 42–46.
[27] R. Messier, A.P. Giri, R.A. Roy, Revised structure zone model for thin film physical structure, J. Vac. Sci. Technol. 2 (1984) 500–503.
[28] S. Chen, R. Zhang, F. Jiang, Y. Li, A primary study on testing the electrical property of arc column in plasma arc welding, J. Manuf. Process. 27 (2017) 276–283.
[29] M. Vicanek, N.M. Ghoniem, The effects of mobility coalescence on the evolution of surface atomic clusters, Thin Solid Films 207 (1992) 90–97.
[30] M. Pfeiler, K. Kutschej, M. Penoy, C. Michotte, C. Mitterer, M. Kathrein, The influence of bias voltage on structure and mechanical/tribological properties of arc evaporated Ti-Al-V-N coatings, Surf. Coat. Technol. 202 (2007) 1050–1054.
[31] R.L. Boxman, S. Goldsmith, Macroparticle contamination in cathodic arc coatings: generation, transport and control, Surf. Coat. Technol. 52 (1992) 39–50.
[32] M. Huang, G. Lin, Y. Zhao, C. Sun, L. Wen, C. Dong, Macro-particle reduction mechanism in biased arc ion plating of TiN, Surf. Coat. Technol. 176 (2003) 109–114.
[33] X.S. Wan, S.S. Zhao, Y. Yang, J. Gong, C. Sun, Effects of nitrogen pressure and pulse bias voltage on the properties of Cr-N coatings deposited by arc ion plating, Surf. Coat. Technol. 204 (2010) 1800–1810.
[34] V.D. Ovcharenko, A.S. Kuprin, G.N. Tolmachova, I.V. Kolodiy, A. Gilewicz, O. Lupicka, J. Rochowicz, B. Warcholinski, Deposition of chromium nitride coatings using vacuum arc plasma in increased negative substrate bias voltage, Vacuum 117 (2015) 27–34.
[35] B. Warcholinski, A. Gilewicz, J. Ratajski, Z. Kuklinski, J. Rochowicz, An analysis of macroparticle-related defects on CrCN and CrN coatings in dependence of the substrate bias voltage, Vacuum 86 (2012) 1235–1239.
[36] D.B. Lewis, S.J. Creasey, C. Wüstefeld, A.P. Ehiasarian, P.E. Hovsepian, The role of the growth defects on the corrosion resistance of CrN/NbN superlattice coatings deposited at low temperatures, Thin Solid Films 503 (2006) 143–148.
[37] S.A. Glatz, R. Hollerweger, P. Polcik, R. Rachbauer, J. Paulitsch, P.H. Mayrhofer, Thermal stability and mechanical properties of arc evaporated Ti-Al-Zr-N hard coatings, Surf. Coat. Technol. 266 (2015) 1–9.
[38] J. Hu, X.b. Tian, H.Y. Liu, C.Z. Gong, Q.W. Tian, M.Z. Wu, M.Q. Li, Enhanced discharge and microstructure of the ta-C coatings by electromagnetically enhanced cathodic arc at argon atmosphere, Surf. Coat. Technol. (2018), https://doi.org/10.1016/j.surfcoat.2018.08.020.
[39] J.A. Freeman, P.J. Kelly, G.T. West, J.W. Bradley, I. Iordanova, The effects of composition and pulsed biasing on chromium nitride films, Surf. Coat.Technol. 204 (2009) 907–910.
[40] R. Franz, J. Neidhardt, R. Kaindl, B. Sartory, R. Tessadri, M. Lechthaler, P. Polcik, C. Mitterer, Influence of phase transition on the tribological performance of arc-evaporated AlCrVN hard coatings, Surf. Coat. Technol. 203 (2009) 1101–1105.
[41] C. Mitterer, P.H. Mayrhofer, J. Musil, Thermal stability of PVD hard coatings, Vacuum 71 (2003) 279–284.
[42] G. Greczynski, J. Lu, J. Jensen, I. Petrov, J.E. Greene, S. Bolz, W. Kölker, Ch. Schiffers, O. Lemmer, L. Hultman, Strain-free, single-phase metastable $Ti_{0.38}Al_{0.62}N$ alloys with high hardness: metal-ion energy vs. momentum effects during film growth by hybrid high-power pulsed/dc magnetron cosputtering, Thin Solid Films 556 (2014) 87–98.
[43] H. Ezura, K. Ichijo, H. Hasegawa, K. Yamamoto, A. Hotta, T. Suzuki, Micro-hardness, microstructures and thermal stability of (Ti,Cr,Al,Si)N films deposited by cathodic arc method, Vacuum 82 (2008) 476–481.
[44] S. Zhang, L. Wang, Q. Wang, M. Li, A superhard CrAlSiN superlattice coating deposited by multi-arc ion plating: I. Microstructure and mechanical properties, Surf. Coat. Technol. 214 (2013) 160–167.

[45] L. Wei, F. Mei, N. Shao, M. Kong, G. Li, J. Li, Template-induced crystallization of amorphous SiO_2 and its effects on the mechanical properties of TiN/SiO_2 nano-multilayers, Appl. Phys. Lett. 86 (2005) 889–892.
[46] R. Hahn, M. Bartosik, R. Soler, C. Kirchlechner, G. Dehm, P.H. Mayrhofer, Superlattice effect for enhanced fracture toughness of hard coatings, Scripta Mater 124 (2016) 67–70.
[47] L. Huang, H. Xu, R. Zhang, X. Cheng, J. Xia, Y. Xu, H. Li, Synthesis and characterization of g-C_3N_4/MoO_3 photocatalyst with improved visible-light photoactivity, Appl. Surf. Sci. 283 (2013) 25–32.
[48] C. Rebholz, H. Ziegele, A. Leyland, A. Matthews, Structure, mechanical and tribological properties of nitrogen-containing chromium coatings prepared by reactive magnetron sputtering, Surf. Coat. Technol. 115 (1999) 222–229.
[49] Y. Ye, Y. Wang, C. Wang, J. Li, Y. Yao, An analysis on tribological performance of CrCN coatings with different carbon contents in seawater, Tribol. Int. 91 (2015) 131–139.
[50] X. Liu, L. Wang, Z. Lu, Q. Xue, Vacuum tribological performance of DLC-based solid–liquid lubricating coatings: influence of sliding mating materials, Wear 292 (2012) 124–134.
[51] Z. Yan, D. Jiang, X. Gao, M. Hu, D. Wang, Y. Fu, J. Sun, D. Feng, L. Weng, Friction and wear behavior of TiN films against ceramic and steel balls[J], Tribol. Int. 124 (2018) 61–69.
[52] Z. Li, H. Zhang, W. He, L. Xu, G. Zhang, X. Nie, B. Liao, Y. Li, Tribological performance of GLC, WC/GLC and TiN films on the carburized M50NiL steel, Surf. Coat. Technol. 361 (2019) 1–8.
[53] E. Badisch, G.A. Fontalvo, C. Mitterer, The response of PACVD TiN coatings to tribological tests with different counterparts, Wear 256 (2004) 95–99.
[54] S.Y. Yoon, J.K. Kim, K.H. Kim, A comparative study on tribological behavior of TiN and TiAlN coatings prepared by arc ion plating technique, Surf. Coat. Technol. 161 (2002) 237–242.
[55] W. Heinke, A. Leyland, A. Matthews, G. Berg, C. Friedrich, E. Broszeit, Evaluation of PVD nitride coatings, using impact, scratch and Rockwell-C adhesion tests, Thin Solid Films 270 (1995) 431–438.
[56] J. Lin, J.J. Moore, W.D. Sproul, B. Mishra, Z. Wu, Modulated pulse power sputtered chromium coatings, Thin Solid Films 518 (2009) 1566–1570.
[57] Y.Q. Fu, H.J. Du, W.M. Huang, S. Zhang, M. Hu, TiNi-based thin films in MEMS applications: a review, Sens. Actuators. A. Phys. 112 (2004) 395–408.